Chemical Science

ROYAL SOCIETY OF CHEMISTRY

EDGE ARTICLE

View Article Online
View Journal | View Issue

Cite this: *Chem. Sci.*, 2025, **16**, 2391

All publication charges for this article have been paid for by the Royal Society of Chemistry

$Li_{1.6}AlCl_{3.4}S_{0.6}$: a low-cost and high-performance solid electrolyte for solid-state batteries†

Tej P. Poudel, ‡[abe] Ifeoluwa P. Oyekunle, ‡[be] Michael J. Deck, [be] Yudan Chen, [be] Dewen Hou, [c] Pawan K. Ojha, [be] Bright O. Ogbolu, [be] Chen Huang, [ab] Hui Xiong [d] and Yan-Yan Hu *[abe]

Solid electrolytes (SEs) are crucial for advancing next-generation rechargeable battery technologies, but their commercial viability is partially limited by expensive precursors, unscalable synthesis, or low ionic conductivity. Lithium tetrahaloaluminates offer an economical option but exhibit low Li^+ conductivities with high activation energy barriers. This study reports the synthesis of lithium aluminum chalcohalide ($Li_{1.6}AlCl_{3.4}S_{0.6}$) using inexpensive precursors *via* one-step mechanochemical milling. The resulting Cl–S mixed-anion sublattice significantly improves the ionic conductivity from 0.008 mS cm^{-1} for $LiAlCl_4$ to 0.18 mS cm^{-1} for $Li_{1.6}AlCl_{3.4}S_{0.6}$ at 25 °C. Structural refinement of the high-resolution XRD patterns and ^6Li magic-angle-spinning (MAS) NMR quantitative analysis reveals the formation of tetrahedrally-coordinated, face- and edge-shared $LiCl_xS_y$ octahedra that facilitate 3D Li^+ transport. *Ab initio* molecular dynamics (AIMD) simulations on $Li_{1.6}AlCl_{3.4}S_{0.6}$ support an enhanced 3D network for Li^+ migration with increased diffusivity. All-solid-state battery (ASSB) half-cells using $Li_{1.6}AlCl_{3.4}S_{0.6}$ exhibit high-rate and long-term stable cycling performance. This work highlights the potential of $Li_{1.6}AlCl_{3.4}S_{0.6}$ as a cost-effective and high-performance SE for ASSBs.

Received 21st October 2024
Accepted 31st December 2024

DOI: 10.1039/d4sc07151d

rsc.li/chemical-science

Introduction

All-solid-state batteries (ASSBs) are rapidly gaining traction due to their high energy density and enhanced safety features, positioning them as strong contenders to replace traditional liquid-electrolyte-based lithium-ion batteries (LIBs) in portable electronic devices and electric vehicles.[1,2] The practical commercialization of ASSBs hinges on discovering SEs that satisfy the cost and performance metrics. In recent years, ternary halides such as $LiAlCl_4$ and $NaAlCl_4$ have received significant attention owing to their low cost and fast ion transport when in solution or as a melt.[3–6]

Aluminum is the third most abundant element in the earth's crust,[7] which makes it a desirable lost-cost component in SEs for ASSBs. However, despite recent advancements in enhancing Li^+ dynamics within the lithium tetrahaloaluminate class of solid electrolytes, their ionic conductivity remains notably low, thereby restricting their practical applications in ASSBs. Recent computational studies have demonstrated that stabilizing a metastable phase of $LiAlCl_4$ can force Li-ions to occupy interstitial sites, thereby reducing the activation energy barrier for ion transport. Specifically, mechanochemical synthesis has induced structural disorder in $LiAlCl_4$, resulting in a small fraction (2.5%) of Li-ions occupying interstitial tetrahedral sites.[8] This has significantly improved the ionic conductivity of $LiAlCl_4$ to 0.02 mS cm^{-1} at 25 °C, compared to the previous value of 0.001 mS cm^{-1}.[9] However, this improvement is still insufficient for commercial applications in ASSBs, which require conductivities greater than 0.1 mS cm^{-1} at 25 °C.

A synthesis approach that does not require high-temperature heating is highly attractive for fabricating commercially viable SEs. For example, by subjecting $LiAlBr_4$ to mechanical stress, a moderate ionic conductivity of 0.033 mS cm^{-1} at room temperature has been reported.[3] Li^+ transport within this material is facilitated *via* octahedral and tetrahedral interstitial sites, which are intrinsic to lithium tetrahaloaluminates.[3,8] Previous studies have shown that for some Li-SEs, *e.g.*, Li_6PS_5Cl, Li_3PS_4, and $LiAlCl_4$, ionic conductivity can be enhanced by introducing local disorder within the anion sublattice.[10–17] Moreover, studies have reported connecting non-accessible ion-conducting channels by a random distribution of cations in

[a]*Materials Science and Engineering Program, The Graduate School, Florida State University, 2005 Levy Ave., Tallahassee, FL 32310, USA. E-mail: yhu@fsu.edu*

[b]*Department of Chemistry and Biochemistry, Florida State University, 95 Chieftan Way, Tallahassee, FL 32306, USA*

[c]*Center for Nanoscale Materials, Argonne National Laboratory, 9700 S Cass Ave, Lemont, IL 60439, USA*

[d]*Micron School of Materials Science and Engineering, Boise State University, Boise, ID, 83725, USA*

[e]*Center of Interdisciplinary Magnetic Resonance, National High Magnetic Field Laboratory, 1800 East Paul Dirac Drive, Tallahassee, FL 32310, USA*

† Electronic supplementary information (ESI) available. See DOI: https://doi.org/10.1039/d4sc07151d

‡ Authors contributed equally.

a host structure *via* local disorder.[18] To further improve the ionic conductivity, local disorder on the atomic scale can be implemented.[19]

Herein, we demonstrate an effective approach for improving Li^+ conduction in $LiAlCl_4$ by mixing inexpensive and poor-conducting Li_2S and $AlCl_3$. An ionic conductivity of 0.18 mS cm^{-1} is achieved at 25 °C for $Li_{1.6}AlCl_{3.4}S_{0.6}$ compared to 0.008 mS cm^{-1} for $LiAlCl_4$. Powder X-ray diffraction and solid-state nuclear magnetic resonance (NMR) spectroscopy, combined with *Ab initio* molecular dynamics (AIMD) simulations, were utilized to determine the structural origin of the improved ionic conductivity in $Li_{1.6}AlCl_{3.4}S_{0.6}$. Galvanostatic measurements of $Li_{1.6}AlCl_{3.4}S_{0.6}$-containing ASSB half-cells show an improved rate performance and long-term cycling stability compared with the control cell utilizing $LiAlCl_4$.

Experimental

Material synthesis

LiCl (Sigma-Aldrich) was dried at 200 °C for 12 hours under a dynamic vacuum before being stored in an argon-filled glovebox. Anhydrous Li_2S (Alfa Aesar) and ultra-dry $AlCl_3$ (Alfa Aesar) were used as received and handled under argon. Stoichiometric amounts of precursors were ground using a mortar/pestle for 5 minutes inside an argon-filled glovebox. The hand-milled powder was transferred into a ZrO_2 jar containing two 10 mm balls as milling media. After the jar was vacuum sealed, mechanochemical mixing was performed using a SPEX 8000M MIXER/MILL (SPEX®SamplePrep, USA) for 20 hours. Afterward, the ball-milled powder, typically ~130 mg, was pressed into a pellet of 8 mm in diameter under ~400 MPa inside an argon-filled Mbraun glovebox. The resulting pellet had a thickness of ~1.2 mm and appeared shiny white.

Powder X-ray diffraction. The as-milled samples were packed in a zero-background sample holder. KAPTON® film (DUPONT™, USA) was used to seal the samples to prevent exposure to humid air. Powder X-ray Diffraction (PXRD) was performed using a RIGAKU® Smartlab powder diffractometer with Bragg-Brentano geometry at a voltage of 45 kV and current of 40 mA with Cu-Kα radiation (a = 1.540 562 Å). The data was collected in the 2θ range of 10–80° at a step size of 0.03° for 30 minutes.

Synchrotron X-ray diffraction. Synchrotron X-ray diffraction (SXRD) measurements were carried out in the transmission mode at the 17-BM-B beamline, APS, at Argonne National Lab (ANL), Illinois. The exact X-ray wavelength was refined to 0.24117 Å. The sample was loaded inside a special glass capillary, and the holder was moved up and down during tests to ensure uniformity of the measured results.

Rietveld refinement. Rietveld refinement of the lab and synchrotron PXRD data was performed using the GSAS-II software. Structural analysis of the synchrotron PXRD data on $LiAlCl_4$ and Li_2AlCl_3S reveals a monoclinic phase belonging to the $P2_1/c$ space group of $LiAlCl_4$ (ICSD – 35275). Sulfur occupancy was tested on all the chlorine sites, and the result was only considered accurate when sulfur occupancy was greater than 1% on the tested site. Lithium and aluminum occupancy were tested for the counter-cation sites of each other to find the most probable structure. Atomic parameters for the site were fixed for the substituents (S, Cl, *etc.*).

Computational approach. All density functional theory (DFT) energy calculations and *ab initio* molecular dynamics (AIMD) simulations were carried out in the Vienna *ab initio* simulation package (VASP).[20] The projector-augmented-wave (PAW) approach was used.[21] Perdew–Burke–Ernzerhof generalized-gradient approximation (GGA-PBE) was chosen as the exchange-correlation functional using the latest PAW potential files available in VASP.[22] Python Materials Genomics (Pymatgen) package[23] was used to optimize the structures of Li_2AlCl_3S. 10 supercells with different local environments were generated based on the 2 × 2 × 1 supercell of the LACS obtained from the high-resolution XRD structure refinement. Geometry optimization of the generated supercells was carried out using DFT calculations. The AIMD simulations[24] were based on the canonical ensemble for over 80 ps with a time step of 2 fs. The temperature was initialized at 100 K and elevated to the target value for the simulations.

Solid-state NMR. ^6Li and ^7Li NMR experiments were performed using a Bruker Advance-III 500 spectrometer at Larmor frequencies of 73.6 MHz and 194.4 MHz for ^6Li and ^7Li, respectively. The magic-angle-spinning (MAS) rate was 24 kHz. Single-pulse MAS ^6Li and ^7Li NMR experiments were performed using $\pi/2$ pulse lengths of 3.30 μs and 2.90 μs, respectively. For Li_2AlCl_3S, the recycle delays were 500 s for ^6Li and 80 s for ^7Li, while recycle delays of 500 s for ^6Li and 90 s for ^7Li was utilized for $LiAlCl_4$. ^7Li NMR spectra were calibrated with LiCl(s) at −1.1 ppm, and ^7Li T_1 relaxation time was measured with an inversion-recovery pulse sequence.

Variable-temperature ^7Li T_1 relaxation NMR experiments were performed using a Bruker Avance-I 300 MHz Spectrometer from 25 to 70 °C. An inversion recovery pulse sequence with a $\pi/2$ pulse length of 2.63 μs was utilized. The ^7Li Larmor frequency was 116.6 MHz. Sample powders were packed into 4 mm ZrO_2 rotors under Argon and spun at a MAS rate of 10 kHz.

A $^6Li|SE|^6Li$ symmetrical cell was assembled in an argon-filled glovebox for the $^6Li \rightarrow {}^7Li$ tracer exchange experiments. The cell was then subjected to galvanostatic cycling for 3 days at a current density of 5 μA cm^{-2} to drive the diffusion of $^6Li^+$ ions from the ^6Li foil into the Li_2AlCl_3S pellet. Following the galvanostatic cycling, ^6Li MAS NMR experiments were performed on the cycled Li_2AlCl_3S pellet using the Bruker Advance-III 500 spectrometer at a spinning rate of 24 kHz, using the same parameters described above.

Electrochemical impedance spectroscopy (EIS). The samples were pressed in a mold of 8 mm diameter to make 1.3 mm thick pellets, which were sandwiched between indium of diameter 6 mm (about 0.24 in) followed by stainless steel plungers as ion-blocking electrodes. EIS measurement was carried out on a Biologic SP-300 electrochemical analyzer within a frequency range from 7 MHz to 1 Hz using a voltage of 10 mV. The conductivities are calculated using resistance obtained by fitting the Nyquist plots using an equivalent circuit model. Variable-temperature EIS characterization was performed in the CSZ microclimate chamber from −20 °C to 70 °C using

a Biologic SP-300, and Arrhenius-type plots were used to calculate the activation energies and Arrhenius prefactors.

Direct current (DC) polarization. The DC polarization method was used to measure the electronic conductivity.[25] In-house-built split cells (diameter = 8 mm) using PEEK insulating cylinder and stainless-steel plungers as current collectors and indium foils (~6 mm diameter) as ion-blocking electrodes were used.

Cyclic voltammetry (CV), linear sweep voltammetry (LSV), and galvanostatic cycling of ASSB half-cells. ASSB half-cells were assembled using pressure cells constructed in-house, using a PEEK casing of 10 mm diameter and stainless-steel plungers. For CV measurements, the initial steps involved pressing 100 mg of $LiAlCl_4$ (or Li_2AlCl_3S) at 300 MPa for 10 s. Then, roughly 10 mg of the manually mixed 3SE : carbon black (C: Super P) composite was evenly spread and pressed at 300 MPa for 10 s. On the opposite side of the $LiAlCl_4$ (or Li_2AlCl_3S) pellet, a piece of indium (In) foil measuring 5/16 inch in diameter and 0.1 mm in thickness, with an approximate weight of 32 mg was attached. Subsequently, lithium foil with a 3/16-inch diameter and weighing around 1 mg was pressed onto the In foil to form Li–In and used as the counter electrode, giving a final cell setup of Li–In|SE|3SE:C. With the cell sealed using vacuum grease, it was subjected to electrochemical cycling under an estimated stack pressure of approximately 30 MPa at 22 °C. CV and LSV measurements were conducted with a scan rate of 0.2 mV s^{-1} from 0 to 4 V *vs.* Li–In and 0 to 4.5 V respectively.

To prepare the composite cathode (or catholyte) for galvanostatic cycling, spherical TiS_2 particles of ~74 microns were purchased from Sigma-Aldrich. It was dried at 200 °C for 12 hours, then subjected to ball milling for 5 hours at 300 rpm to reduce particle size. Subsequently, $LiAlCl_4$ or Li_2AlCl_3S was combined with TiS_2 at a TiS_2 : SE mass ratio of 1 : 2 and ground together using a mortar and pestle for 10 minutes. Li_6PS_5Cl, synthesized following the established method by Patel *et al.*,[13] was pressed into pellets at 300 MPa for 10 seconds as the separator. For the half-cell assembly, 12 mg of the catholyte was evenly spread onto one side of the Li_6PS_5Cl pellet, achieving an aerial loading of approximately 1.25 mA h cm^{-2}, followed by further pressing at 300 MPa for 10 seconds. A Li–In alloy foil was affixed to the opposite side of the Li_6PS_5Cl pellet to assemble the Li–In|Li_6PS_5Cl|2SE:TiS_2 (SE: $LiAlCl_4$ or Li_2AlCl_3S) half cells. Finally, the cells were sealed with vacuum grease and subjected to controlled cycling conditions at 22 °C with a stack pressure of ~30 MPa, within a voltage window of 1–2.5 V *vs.* Li–In. For rate performance evaluations, the cells underwent cycling for 5 cycles at each of the following rates: 0.1C, 0.2C, 0.5C, 1C, and 2C, with C representing the charge–discharge rate. Correspondingly, these rates translate to current densities of 0.14 mA cm^{-2}, 0.28 mA cm^{-2}, 0.70 mA cm^{-2}, 1.40 mA cm^{-2}, and 2.80 mA cm^{-2}, respectively. Subsequently, long-term stability testing was conducted over 175 cycles at 0.2C.

Results and discussion

X-ray diffraction and structure

X-ray diffraction (XRD) was employed to investigate the long-range structure of the synthesized solid electrolytes. The powder XRD confirms the presence of a monoclinic $LiAlCl_4$ phase (Fig. 1). With sulfur substitution, the long-range monoclinic structure is maintained for Li_2AlCl_3S. However, the weak and diffuse diffraction pattern of the as-milled Li_2AlCl_3S suggests a decrease in the crystallinity of the material. Rietveld refinement was performed against high-resolution XRD data using GSAS-II. Fig. 1(c)–(f) shows the diffraction patterns and the refined structures. For $LiAlCl_4$, the crystalline phase was refined with a monoclinic structure type in the $P2_1/c$ space group. The structure is built from distorted LiX_6 octahedra and $AlCl_4^-$ tetrahedra. Two $LiCl_6^{5-}$ octahedra are edge-shared to form $Li_2Cl_{10}^{8-}$ dimers.[1] $AlCl_4^-$ tetrahedra are isolated from one another. All the atoms in the structure occupy only the 4e Wyckoff positions, leaving all other sites, *i.e.*, 2a, 2b, 2c, and 2d Wyckoff positions, vacant (see Fig. 1(e)). The arrangement of atoms is characterized by a slightly distorted hexagonal cubic packed (*hcp*) Cl^- sublattice, where Li^+ and Al^{3+} fill octahedral and tetrahedral interstices, respectively.[1] In addition, each $AlCl_4$ tetrahedron is linked to one Li–Cl dimer *via* two edges and to two other dimers through one corner each (Fig. 1(e)).

Similarly, Li_2AlCl_3S crystallizes in the $P2_1/c$ space group. However, different from $LiAlCl_4$, the unit cell consists of three octahedrally coordinated cation sites – Li1 at 4e, Li2 at 2a, and Li3 at the 2a Wyckoff positions; and tetrahedrally coordinated Al at the 4e Wyckoff position. Sulfur and chlorine atoms co-occupy the 4e anionic site, yielding a disordered anion sublattice. Along the *c*-direction, the structure exhibits three distinct cation layers (Fig. 1(g)). In the first layer, Li2 octahedra $(LiCl_6)^{5-}$ edge-share with Li1 $(LiCl_{5.4}S_{0.6})^{5.6-}$ and corner-share with the tetrahedrally coordinated Al. In the second layer, Li3 octahedra $(LiCl_{4.8}S_{1.2})^{6.2-}$ face-share with Li1 (Fig. 1(h)), and both Li1 and Li3 octahedra share corners with the tetrahedrally coordinated Al. In the third layer, the Al sites face-share with Li3 and edge-share with Li1 and Li2 octahedra. In addition, the edge-sharing Li1, Li2, and Li3 octahedra produce tetrahedral voids (Fig. 1(f)). The complete refinement parameters for $LiAlCl_4$ and Li_2AlCl_3S are provided in Tables S1 to S3.† The refinement reveals the actual composition of the nominal Li_2AlCl_3S is $Li_{1.6}AlCl_{3.4}S_{0.6}$, which exhibits mixed Cl^-/S^{2-} site occupancies in the structure. Consistent with the refined composition, a trace amount of Li_2S is identified in the ball-milled sample. The refined composition, $Li_{1.6}AlCl_{3.4}S_{0.6}$, is adopted hereafter.

Solid-state NMR

To understand the local structures of $LiAlCl_4$ and $Li_{1.6}AlCl_{3.4}S_{0.6}$, ^6Li MAS NMR experiments were performed. As shown in Fig. 2, the ^6Li MAS NMR spectrum of $LiAlCl_4$ reveals a major resonance at −0.92 ppm assigned to octahedrally coordinated Li1. This is consistent with findings from a previous study.[8] In addition, a minor resonance at −1.08 ppm is assigned to LiCl.[26] After incorporating S^{2-} in the parent material, the ^6Li NMR spectra of $Li_{1.6}AlCl_{3.4}S_{0.6}$ is characterized by five distinct resonances at −0.89, −1.24, −0.07, 1.48, and 2.21 ppm – indicating changes in the local Li environment. The minor peak observed at 2.21 ppm corresponds to the Li_2S impurity.[27] The phase

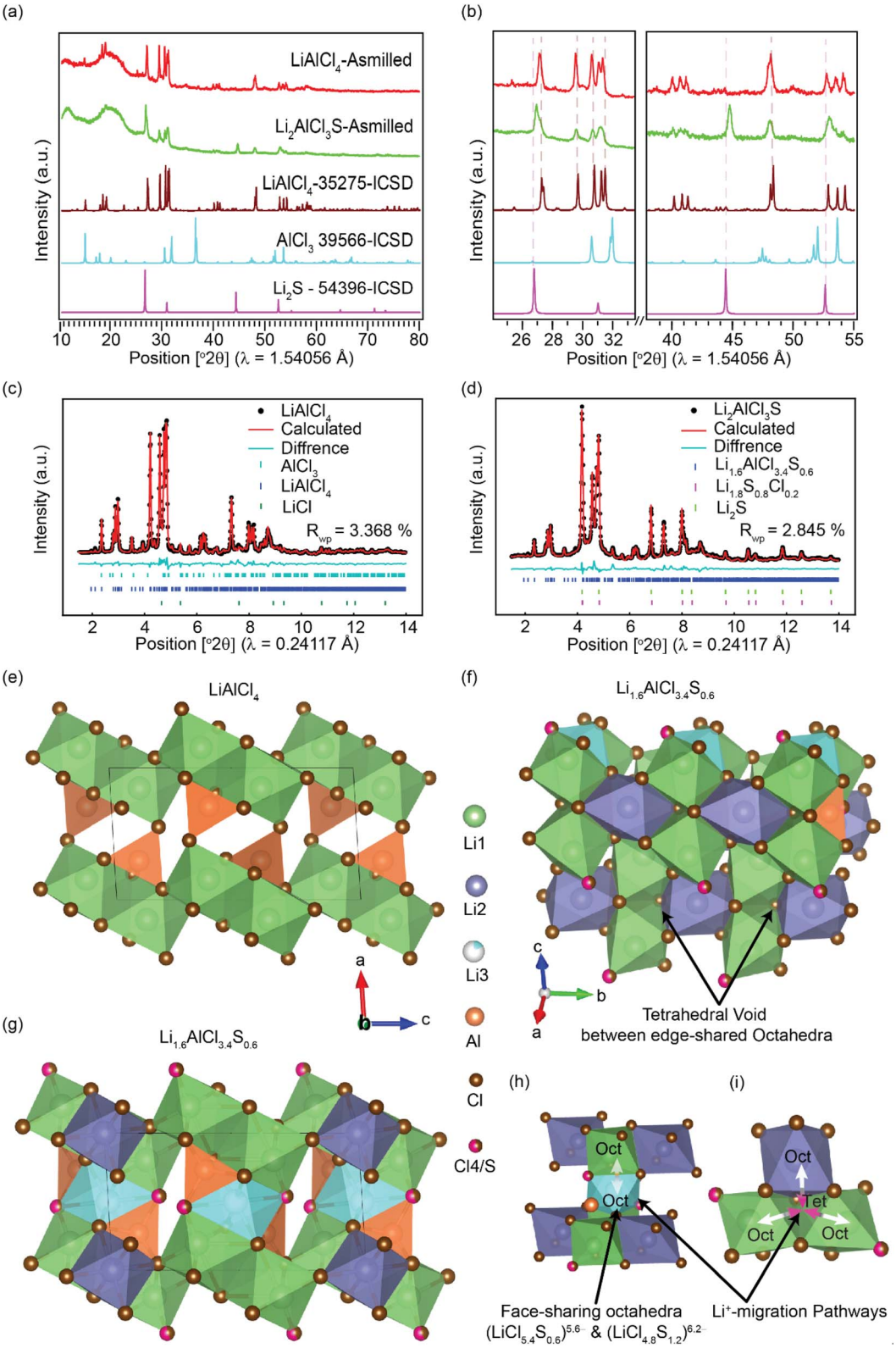

Fig. 1 Long-range structures of $LiAlCl_4$ and Li_2AlCl_3S, determined using lab-X-ray diffraction and high-resolution X-ray diffraction. (a) Lab X-ray diffraction patterns of the as-milled $LiAlCl_4$ and Li_2AlCl_3S. The ICSD patterns of precursors and $LiAlCl_4$ monoclinic phase ($P2_1/c$ space group) are shown as references. (b) The magnified view of the selected 2θ ranges in (a). (c) and (d) High-resolution X-ray diffraction patterns and the corresponding Rietveld refinement of $LiAlCl_4$ and Li_2AlCl_3S, respectively. (e) and (g) Monoclinic structures of $LiAlCl_4$ and $Li_{1.6}AlCl_{3.4}S_{0.6}$ with the $P2_1/c$ space group, respectively, obtained from refined high-resolution XRD patterns. (f) The structure of $Li_{1.6}AlCl_{3.4}S_{0.6}$ viewed along the a-axis showing tetrahedral voids face-shared with Li-octahedra. (h) The visualization of partially occupied octahedral lithium at Wyckoff 2b position face-shared with highly distorted octahedral sites at Wyckoff 4e positions. (i) Possible lithium migration pathways.

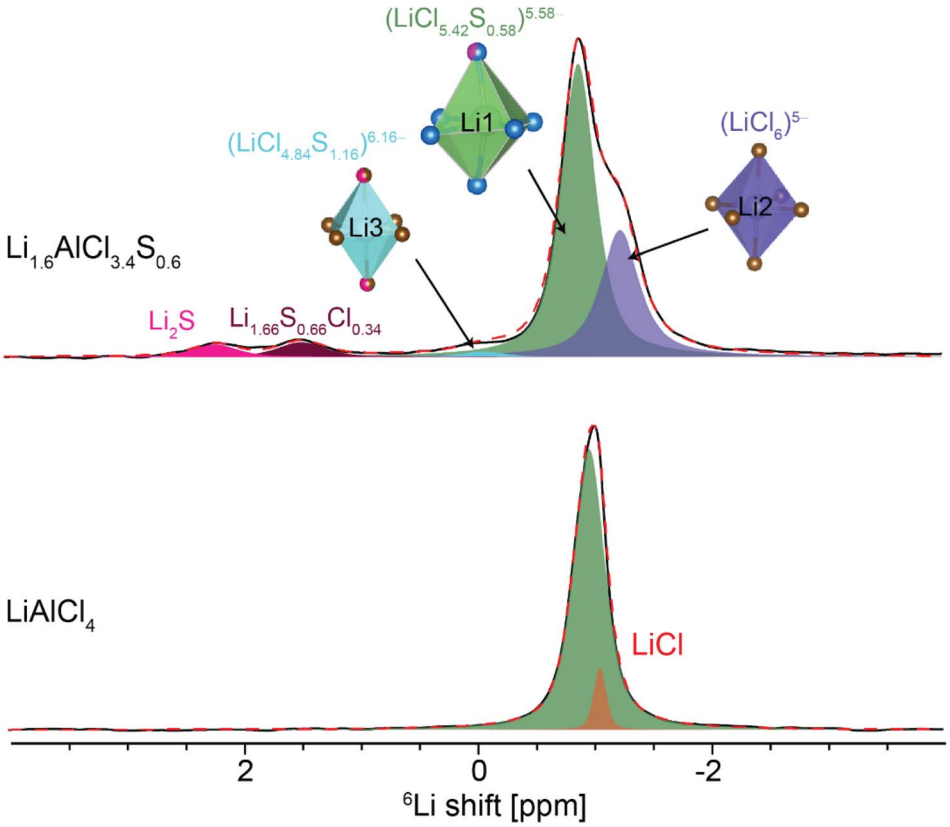

Fig. 2 ^{6}Li MAS NMR spectra of $LiAlCl_4$ and $Li_{1.6}AlCl_{3.4}S_{0.6}$.

quantification is given in Table S4.† The resonances at −0.89, −1.24, and −0.07 ppm are assigned to the octahedrally coordinated Li1, Li2, and Li3 sites, respectively – in agreement with the results from structural refinement. In addition, there is an extra peak at 1.48 ppm, likely from the $Li_{1.66}S_{0.66}Cl_{0.34}$ phase identified with the Rietveld refinement of the high-resolution diffraction pattern (Fig. S1†).

^{7}Li spin–lattice relaxation time (T_1) is a useful indicator of ion dynamics.[11,28] According to the Bloembergen, Purcell, and Pound (BPP) model, T_1 relaxation time is a function of motional rate (τ_c^{-1}),[29] $\frac{1}{T_1} = \frac{3\gamma^4\hbar^2}{10r_0^6}\left[\frac{\tau_c}{1+\omega_0^2\tau_c^2} + \frac{4\tau_c}{1+4\omega_0^2\tau_c^2}\right]$, where γ is the gyromagnetic ratio, $\hbar$ is the reduced Planck's constant, r_0 is the interatomic distance, $\omega_0 = \gamma B_0$ is the Larmor frequency, and B_0 is the external magnetic field strength.

In the fast-motion regime ($\omega_0\tau_c \ll 1$), T_1 increases with increasing motional rate, while in the slow-motion regime ($\omega_0\tau_c \gg 1$), T_1 decreases with increasing motional rate. In addition, a resonance can lie in the intermediate region where $\omega_0\tau_c \approx 1$.[29] Variable-temperature ^{7}Li NMR T_1 relaxation data of $Li_{1.6}AlCl_{3.4}S_{0.6}$ in Fig. S2† reveals a decrease in T_1 relaxation time with increasing temperature and, thus, suggesting Li^+ dynamics in $Li_{1.6}AlCl_{3.4}S_{0.6}$ lie in the slow-motion regime ($\omega_0\tau_c \ll 1$). Therefore, a shorter T_1 value will correlate with faster ion mobility. As presented in Table 1, the ^{7}Li T_1 relaxation time significantly decreases from $LiAlCl_4$ to $Li_{1.6}AlCl_{3.4}S_{0.6}$, suggesting enhanced Li^+ mobility[30] with sulfur incorporation.

Table 1 ^{7}Li spin–lattice relaxation time (T_1) of $LiAlCl_4$ and $Li_{1.6}AlCl_{3.4}S_{0.6}$

Sample	^{7}Li T_1 [s]
$LiAlCl_4$	5.2
$Li_{1.6}AlCl_{3.4}S_{0.6}$	3.1

Ion transport pathways determined by tracer-exchange NMR

To directly probe the Li^+ transport pathways in $Li_{1.6}AlCl_{3.4}S_{0.6}$, tracer-exchange NMR is employed.[31] By identifying and quantifying $^{6}Li^+ \rightarrow {}^{7}Li^+$ exchange under an applied biased potential, the preferential pathway utilized by Li^+ ions for migration is directly mapped out – facilitating the identification of active sites for Li^+ transport.[31–34] The experimental configuration involves sandwiching $Li_{1.6}AlCl_{3.4}S_{0.6}$ pellet between two ^{6}Li foils. An externally applied potential gradient establishes a driving force for $^{6}Li^+$ ions in the ^{6}Li foils to move toward and exchange with $^{7}Li^+$ in the $Li_{1.6}AlCl_{3.4}S_{0.6}$ pellet. Consequently, the preferential Li^+ transport pathways are selectively enriched with $^{6}Li^+$ ions. The ^{6}Li NMR of the pristine and tracer-exchanged $Li_{1.6}AlCl_{3.4}S_{0.6}$ pellet is displayed in Fig. S3a,† and the quantification of the Li sites before and after the tracer-exchange experiment is presented in Fig. S3b.† The ^{6}Li NMR spectra reveal changes in the relative intensities of resonances assigned to distinct Li^+ environments. Notably, a significant increase in the intensity of the Li1 and Li2 resonances is observed, suggesting the major

involvement of Li1 and Li2 in ion conduction. In addition, the Li3 resonance shows a small intensity enhancement after cycling. The enhancement of these resonances suggests that Li1, Li2, and Li3 all participate in Li^+-ion transport within the $Li_{1.6}AlCl_{3.4}S_{0.6}$ solid electrolyte.

AIMD simulations

To further understand the effect of Cl–S anion mixing on the Li^+ density distribution and diffusion, AIMD simulations are employed for $LiAlCl_4$ and $Li_{1.6}AlCl_{3.4}S_{0.6}$ in a $2 \times 2 \times 1$ cell. The mean square displacements (MSD) of Li^+ (Fig. 3(a) and (b)) and distribution probability (Fig. 3(c) and (d)) for Li at 900 K were calculated. The MSD plots demonstrate that Li^+ can diffuse in all three directions, with higher diffusion observed along the *b* direction in $LiAlCl_4$. However, Li^+ diffusion along the *a* and *c* directions increases significantly with Cl–S anion mixing, resulting in comparable MSDs in all three directions in $Li_{1.6}AlCl_{3.4}S_{0.6}$. This transformation indicates that $Li_{1.6}AlCl_{3.4}S_{0.6}$ is a 3D ion conductor with a uniform ion transport network in all three dimensions. Furthermore, the overall MSD of Li^+ shows a 50% increase upon Cl–S anion diversification compared to $LiAlCl_4$. The AIMD simulation of Li^+ trajectories (*i.e.*, Li^+ probability density) in $LiAlCl_4$ shows a localized "cage-like" Li^+ diffusion pattern with few interstitial jumps, indicating limited long-range Li^+ migration. In comparison, $Li_{1.6}AlCl_{3.4}S_{0.6}$ exhibits a delocalized Li^+ diffusion network, suggesting improved macroscopic Li^+ migration and, consequently, enhanced Li^+ conduction in $Li_{1.6}AlCl_{3.4}S_{0.6}$.

Electrochemical properties

To examine ion transport properties of all prepared SEs, variable-temperature electrochemical impedance spectroscopy (EIS) was employed, and the corresponding Nyquist plots at 25 °C are presented in Fig. 4(a) with a corresponding exemplary equivalent circuit fitting shown in Fig. 4(b). The results from the EIS analysis are given in Table 2. Based on fitted resistances from the Nyquist plot using equivalent circuit modeling, the conductivities of $LiAlCl_4$ and $Li_{1.6}AlCl_{3.4}S_{0.6}$ are 0.008 mS cm^{-1} and 0.18 mS cm^{-1}, respectively (Fig. 4(a)). In addition, an ionic conductivity of 0.12 mS cm^{-1} and 0.11 mS cm^{-1} were obtained at $x = 0.5$ and $x = 0.8$ in $Li_{1+x}AlCl_{4-x}S_x$ (Fig. S4†). The lower ionic conductivity observed at $x = 0.5$ is likely due to insufficient sulfur substitution to significantly perturb the lattice and create additional favorable Li^+ migration pathways. Conversely, at $x = 0.8$, the solid-solution limit is reached yielding a high fraction of Li_2S impurity, which likely contributes to the lower ionic conductivity. Therefore, the optimal composition for the highest ionic conductivity is $Li_{1.6}AlCl_{3.4}S_{0.6}$. To confirm the conductivities are due to ionic transport, the DC polarization measurements[25] were performed, and the plots for $LiAlCl_4$ and

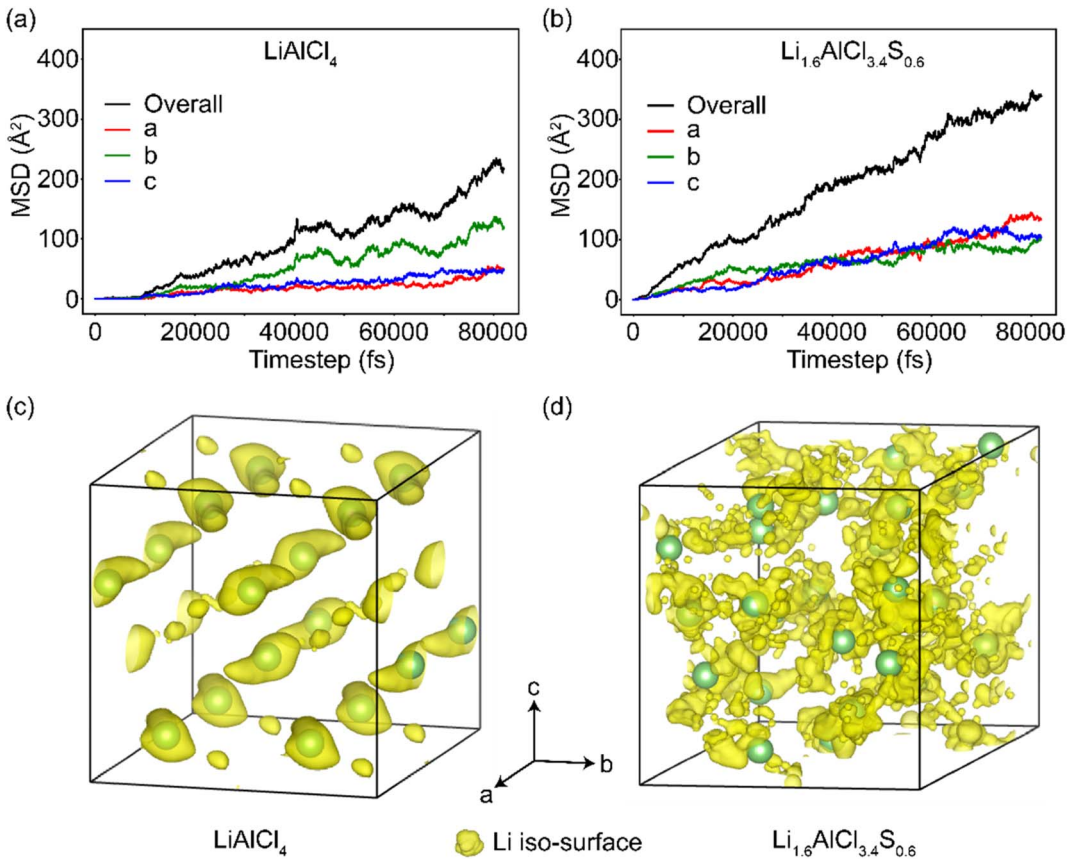

Fig. 3 Mean square displacement (MSD) of Li^+ in (a) $LiAlCl_4$ and (b) $Li_{1.6}AlCl_{3.4}S_{0.6}$ generated from AIMD simulations. Li^+ (yellow) probability density map of $LiAlCl_4$ (c) and $Li_{1.6}AlCl_{3.4}S_{0.6}$ (d) in a $2 \times 2 \times 1$ cell based on AIMD simulations at 900 K.

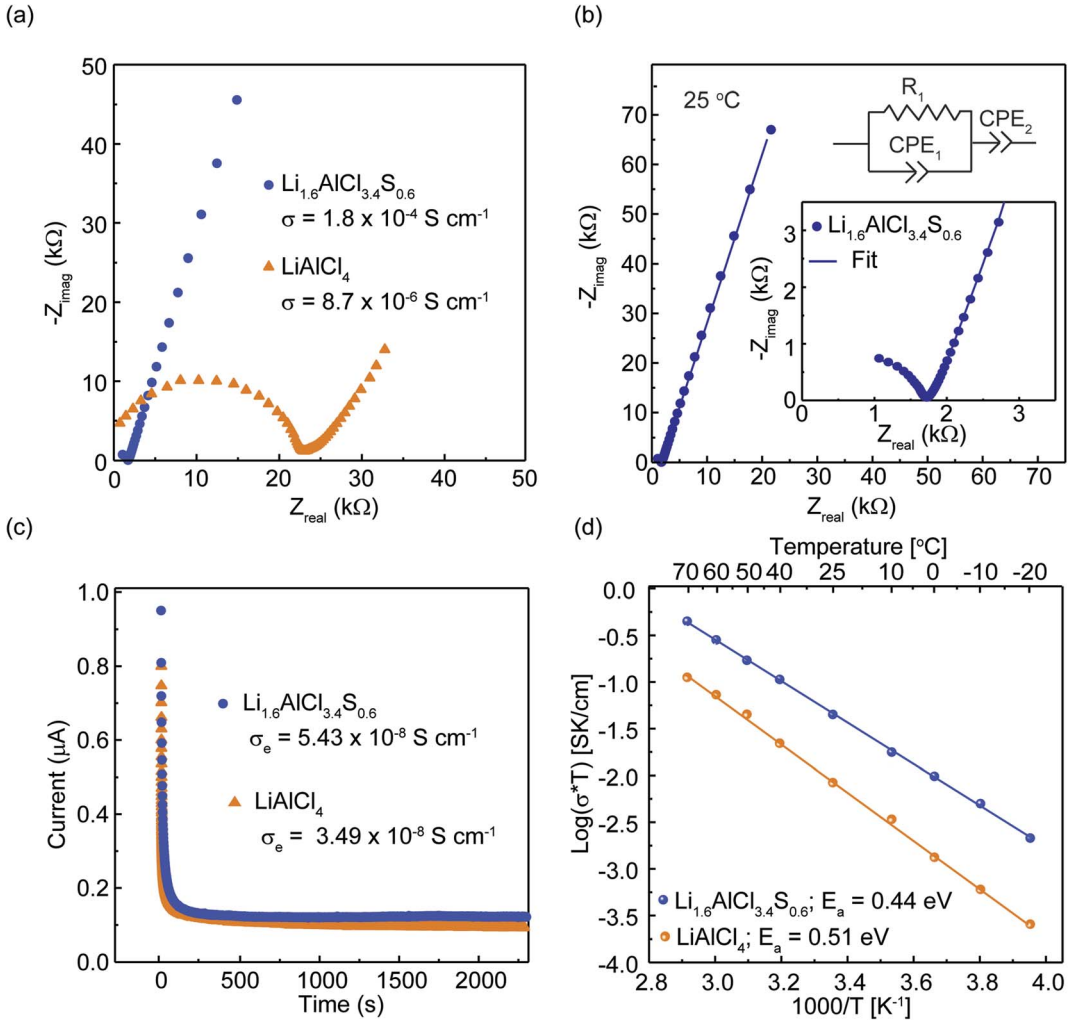

Fig. 4 Charge transport properties of $LiAlCl_4$ and $Li_{1.6}AlCl_{3.4}S_{0.6}$. (a) Nyquist plots of $LiAlCl_4$ and $Li_{1.6}AlCl_{3.4}S_{0.6}$. (b) Exemplary equivalent circuit fitting of the Nyquist plot for $Li_{1.6}AlCl_{3.4}S_{0.6}$ measured at 25 °C. (c) Electronic conductivities were determined using DC polarization, and (d) Arrhenius plots and activation energies for ion transport in $LiAlCl_4$ and $Li_{1.6}AlCl_{3.4}S_{0.6}$.

$Li_{1.6}AlCl_{3.4}S_{0.6}$ are shown in Fig. 4(c). The current value upon plateauing corresponds to electronic conductivities of 3.49×10^{-8} S cm^{-1} and 5.43×10^{-8} S cm^{-1} for $LiAlCl_4$ and $Li_{1.6}AlCl_{3.4}S_{0.6}$, respectively, thereby confirming negligible electronic contribution to the measured total conductivities of the samples. The ionic conductivity of $Li_{1.6}AlCl_{3.4}S_{0.6}$ is approximately twenty-fold greater than $LiAlCl_4$ at room temperature. The significant increase in ionic conductivity of $Li_{1.6}AlCl_{3.4}S_{0.6}$ can be attributed to the local disorder and "Li-stuffing" of the Li3-octahedra that connect with neighboring Li1/Li2 octahedra and the substitution of Cl with more polarizable S anions. The energy barrier for Li-ion transport (E_a) was calculated from the variable-temperature EIS measurements between 0 °C to 70 °C, and representative Nyquist plots are shown in Fig. S5.† The Arrhenius-type plot of $LiAlCl_4$ and $Li_{1.6}AlCl_{3.4}S_{0.6}$ are shown in Fig. 4(d). A decrease in E_a from 0.51 eV to 0.44 eV is observed from $LiAlCl_4$ to $Li_{1.6}AlCl_{3.4}S_{0.6}$. This decrease in activation energy correlates with the increase in ionic conductivity.[35] This trend agrees with the energy barrier obtained from the bond valence site energy (BVSE) calculation (Fig. S6†).

Cyclic voltammetry and galvanostatic cycling of ASSB half-cells

Conventionally, CV measurements were done using stainless steel as the blocking electrode, which fails to accurately measure the oxidation and reduction current of SEs due to the

Table 2 DC ionic conductivity at 25 °C, electronic conductivity at 25 °C, activation energy, and Arrhenius prefactor of $LiAlCl_4$ and $Li_{1.6}AlCl_{3.4}S_{0.6}$

Composition	$\sigma_{DC,\ 25°C}$ [S cm^{-1}]	$\sigma_{e,\ 25°C}$ [S cm^{-1}]	E_a [eV]	Log(σ_0) [S cm^{-1} K]
$LiAlCl_4$	8.65×10^{-6}	3.49×10^{-8}	0.51	6.55
$Li_{1.6}AlCl_{3.4}S_{0.6}$	1.80×10^{-4}	5.43×10^{-8}	0.44	6.07

limited electrical contact area of the SE and the planar ion-blocking electrode.[11,36] To overcome this and estimate the oxidation–reduction reactions of the SE, we performed CV utilizing a 3SE : C (mass ratio) composite cathode in the Li–In|SE|3SE : C half-cell setup.[37–39] In this setup, carbon serves as an electronic conductive medium in the composite cathode, enabling increased SE surface area in electrical contact with the electrode and consequential detection of degradation current.[11,17,36–42] Fig. S7† shows the voltammograms of $Li_{1.6}AlCl_{3.4}S_{0.6}$ with a scanning window of 0–4 V *vs.* Li–In. The first cathodic peak starts at the voltage of 1.03 V *vs.* Li–In. This voltage is assigned to the electrolyte reduction to form Li_2S and $AlCl_3$.[11,17,43] The CV for $Li_{1.6}AlCl_{3.4}S_{0.6}$ indicates the onset oxidation voltage of 2.4 V *vs.* Li–In. This is reasonable as most of the reported sulfide solid electrolytes have a lower stability window than halides ($LiAlCl_4$).[44,45] So, the electrochemical stability window of the prepared $Li_{1.6}AlCl_{3.4}S_{0.6}$ is in the range of 1.03–2.40 V *vs.* Li–In, corresponding to the 1.63–3.00 V *vs.* Li/Li^+. We have also performed LSV measurement (Fig. S8†), which shows the same electrochemical stability window of 1.63–3.00 V *vs.* Li/Li^+

Titanium disulfide (TiS_2) was employed as the cathode active material (CAM) in the half-cell configurations for electrochemical evaluation. Li–In|Li_6PS_5Cl|2($LiAlCl_4$):TiS_2 and Li–In|Li_6PS_5Cl|2($Li_{1.6}AlCl_{3.4}S_{0.6}$):$TiS_2$ cells were fabricated according to previous studies.[11,17] A Li–In anode was employed for enhanced stability against SEs and limited dendrite formation through micropores – reducing the risk of short circuits.[46] Li_6PS_5Cl was utilized as the separator due to its high ionic conductivity and stability against Li metal. The electrochemical performance of these half-cells was assessed through a series of rate capability tests, spanning charging/discharging currents from 0.1C to 2C conducted under galvanostatic conditions at ~22 °C. Each rate was applied over five cycles (0.1C ~0.14 mA cm^{-2}, 0.2C ~0.28 mA cm^{-2}, 0.5C ~0.70 mA cm^{-2}, 1C ~1.40 mA cm^{-2}, and 2C ~2.80 mA cm^{-2}) followed by 125 cycles at 0.2C. A theoretical capacity of 239 mA h g^{-1} for TiS_2 was used to calculate the charge–discharge rates.

Fig. 5(a) illustrates the variation in specific capacity with cycle number for the half-cell configurations, while Fig. 5(b) and (c) display the voltage profiles for select cycles. Initially, the cell incorporating $LiAlCl_4$ demonstrated a discharge capacity of approximately 273 mA h g^{-1} and a charge capacity of 213 mA h g^{-1}, whereas the $Li_{1.6}AlCl_{3.4}S_{0.6}$-containing cell exhibited a comparable initial discharge capacity of 272 mA h g^{-1} and a higher charge capacity of 248 mA h g^{-1} (Fig. 5(a) and (b)). Upon the second discharge, the capacity for the $LiAlCl_4$-based cell declined to 208 mA h g^{-1}, whereas the $Li_{1.6}AlCl_{3.4}S_{0.6}$-based cell showed a reduced yet more stable capacity of 240 mA h g^{-1}, eventually stabilizing around 239 mA h g^{-1} (Fig. 5(a) and (b)). This is likely due to the formation of a stable solid–electrolyte interface (SEI) during the first cycle. The lower capacity observed in the $LiAlCl_4$-based cell is primarily due to its low ionic conductivity of the solid

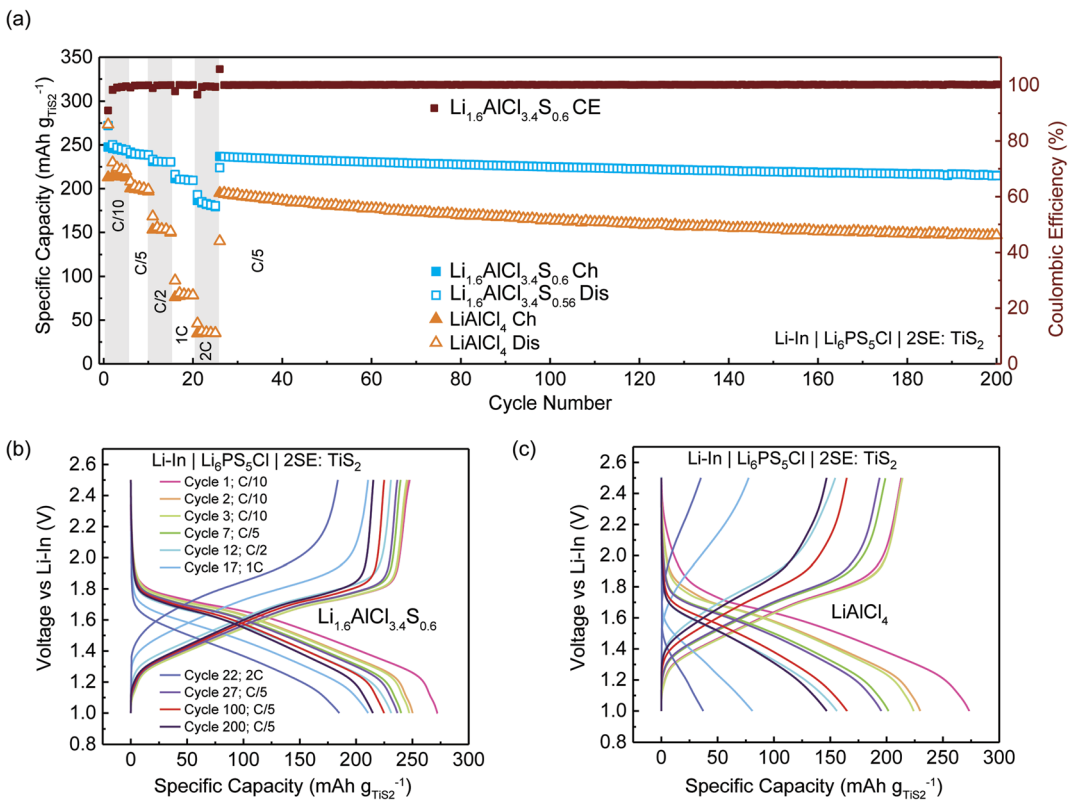

Fig. 5 Galvanostatic cycling of 2SE:TiS_2 catholyte with argyrodite Li_6PS_5Cl as the separator. (a) Rate performance of Li–In|Li_6PS_5Cl|2SE:TiS_2 cell (SE = $LiAlCl_4$ or $Li_{1.6}AlCl_{3.4}S_{0.6}$) followed by long-term cycling at *C*/5, where *C* = 239 mA h g^{-1}. Voltage profile of cycle 1 along with the 2nd cycles of each C-rate for a (b) Li–In|Li_6PS_5Cl|2($Li_{1.6}AlCl_{3.4}S_{0.6}$):$TiS_2$ cell and (c) Li–In| Li_6PS_5Cl|2($LiAlCl_4$):TiS_2 cell.

electrolyte (SE), which restricts the efficient utilization of the active material – leading to a lower capacity.[47] Interestingly, initial capacities recorded for both cells surpassed the theoretical capacity of TiS_2, (239 mA h g^{-1}). This is attributable to the unidentified reversible redox behavior of the SE in addition to the $Ti^{3+/4+}$ redox (Fig. S9†).[48,49]

The $Li_{1.6}AlCl_{3.4}S_{0.6}$-containing cell exhibited a capacity of 180 mA h g^{-1} even at a high discharge rate of 2C, indicative of exceptional rate performance in contrast to the significantly reduced capacity of 37 mA h g^{-1} observed at a similar rate for the $LiAlCl_4$-based cells. Upon returning to 0.2C after 26 cycles, both cell configurations demonstrated remarkable stability over 200 cycles. Furthermore, these cells maintained a high coulombic efficiency exceeding 99% throughout this extended cycle period (Fig. 5(a)). Between the 27th and 200th cycles, the $Li_{1.6}AlCl_{3.4}S_{0.6}$-based cell demonstrated a capacity retention of approximately 90%, whereas the $LiAlCl_4$-based cell exhibited a faster degradation rate. The superior performance of the Li–In|Li_6PS_5Cl|2($Li_{1.6}AlCl_{3.4}S_{0.6}$):$TiS_2$ cell is attributed to the synergistic benefits of enhanced ionic conductivity, electrochemical stability, and improved utilization of cathode active materials.[47]

Conclusion

Developing inexpensive SEs using earth-abundant elements is imperative to reduce the cost of ASSBs for widespread applications in electric vehicles and consumer electronics. In this work, we synthesized a new lithium chalcohalide solid electrolyte, $Li_{1.6}AlCl_{3.4}S_{0.6}$, with a room-temperature ionic conductivity of 0.18 mS cm^{-1}. Structural characterization reveals that the enhanced ionic conductivity of $Li_{1.6}AlCl_{3.4}S_{0.6}$ strongly correlates with the formation of face- and edge-sharing octahedrally coordinated lithium sites, which often create low-energy conduction pathways. AIMD simulations using the refined structures reveal incorporating the optimal amount of S into $LiAlCl_4$ transitions it from a 1D to a 3D conductor. ^{6,7}Li MAS NMR combined with tracer exchange and relaxometry reveals increased ion mobility and participation of all Li^+ sites in ion conduction. $Li_{1.6}AlCl_{3.4}S_{0.6}$ demonstrates good long-term cycling stability and rate performance in ASSBs, achieving a specific capacity of 180 mA h g^{-1} at a fast charging rate of 2C in a Li–In|Li_6PS_5Cl|2($Li_{1.6}AlCl_{3.4}S_{0.6}$):$TiS_2$ battery cell, compared to 37 mA h g^{-1} in the $LiAlCl_4$-containing cell. The cost-effectiveness, combined with the demonstrated high performance, makes $Li_{1.6}AlCl_{3.4}S_{0.6}$ an excellent candidate as electrolytes for ASSBs.

Data availability

The data that supports this manuscript will be available upon request.

Author contributions

Tej Prasad Poudel: data curation: lead; formal analysis: lead; investigation: lead; methodology: lead; software: lead; validation: lead; visualization: lead; writing – original draft: lead. Ifeoluwa P. Oyekunle: data curation: equal; formal analysis: equal; investigation: equal; methodology: equal; software: equal; validation: equal; visualization: equal; writing – original draft: equal. Michael J. Deck: formal analysis: supporting; investigation: supporting; methodology: supporting; validation: supporting; visualization: supporting; writing – original draft: supporting. Yudan Chen: data curation: supporting; formal analysis: supporting; investigation: supporting; methodology: supporting; software: supporting; writing – original draft: supporting. Dewen Hou: data curation: supporting. Pawan K. Ojha: data curation: supporting; formal analysis: supporting; visualization: supporting; writing – review & editing: supporting. Bright O. Ogbolu: validation: supporting; writing – review & editing: supporting. Chen Huang: software: supporting. Hui Xiong: resources: supporting; supervision: supporting; validation: supporting. Yan-Yan Hu, PhD: conceptualization: lead; formal analysis: lead; funding acquisition: lead; methodology: lead; project administration: lead; resources: lead; supervision: lead; validation: lead; visualization: equal; writing – original draft: equal; writing – review & editing: lead.

Conflicts of interest

The authors declare no conflict of interest.

Acknowledgements

The authors acknowledge the support from the National Science Foundation under grant no. DMR-1847038 and DMR-2319151. Hou and Xiong thank the support from the U.S. Department of Energy, Office of Science, Office of Basic Energy Sciences program under Award Number DE-SC0019121. All solid-state NMR experiments were performed at the National High Magnetic Field Laboratory, which is supported by National Science Foundation Cooperative Agreement No. DMR-1644779 and DMR-2128556*. This research used resources of the Advanced Photon Source, a U.S. Department of Energy (DOE) Office of Science user facility operated for the DOE Office of Science by Argonne National Laboratory under Contract No. DE-AC02-06CH11357.

References

1 X. Cao, S. Xu, Y. Zhang, X. Hu, Y. Yan, Y. Wang, H. Qian, J. Wang, H. Chang, F. Cheng and Y. Yang, Fluorine-Doped High-Performance Li6PS5Cl Electrolyte by Lithium Fluoride Nanoparticles for All-Solid-State Lithium-Metal Batteries, *Trans. Tianjin Univ.*, 2024, **30**, 250–261, DOI: 10.1007/s12209-024-00394-1.

2 K. Tuo, C. Sun and S. Liu, Recent Progress in and Perspectives on Emerging Halide Superionic Conductors for All-Solid-State Batteries, *Electrochem. Energy Rev.*, 2023, **6**(17), 1–46, DOI: 10.1007/s41918-023-00179-5.

3 N. Flores-González, N. Minafra, G. Dewald, H. Reardon, R. I. Smith, S. Adams, W. G. Zeier and D. H. Gregory, Mechanochemical Synthesis and Structure of Lithium

Tetrahaloaluminates, $LiAlX_4$ (X = Cl, Br, I): A Family of Li-Ion Conducting Ternary Halides, *ACS Mater. Lett.*, 2021, **3**(5), 652–657, DOI: **10.1021/acsmaterialslett.1c00055**.

4 F. Scholz, W. Unkrig, P. Eiden, M. A. Schmidt, A. Garsuch and I. Krossing, Synthesis, Spectroscopic Characterization, Crystal Structures, Energetics, and Thermal Stabilities of Li $[AlX_4]$ (X = Cl, Br): Investigation and Performance of Their Electrolyte Solutions, *Eur. J. Inorg. Chem.*, 2015, (19), 3128–3138, DOI: **10.1002/ejic.201500254**.

5 T. Gao, B. Wang, L. Wang, G. Liu, F. Wang, H. Luo and D. Wang, $LiAlCl_4 \cdot 3SO_2$ as a High Conductive, Non-Flammable and Inorganic Non-Aqueous Liquid Electrolyte for Lithium Ion Batteries, *Electrochim. Acta*, 2018, **286**, 77–85, DOI: **10.1016/j.electacta.2018.08.033**.

6 J. M. Weller, M. M. Li, E. Polikarpov, K. S. Han, N. Kidner, A. Patel, M. Nguyen, M. Stout, M. Gossett, K. Jung, D. M. Reed, V. L. Sprenkle and G. Li, Unlocking the NaCl-$AlCl_3$ Phase Diagram for Low-Cost, Long-Duration Na-Al Batteries, *Energy Storage Mater.*, 2023, **56**, 108–120, DOI: **10.1016/j.ensm.2023.01.009**.

7 J. M. S. D. Campos and L. F. Viccini, Cytotoxicity of Aluminum on Meristematic Cells of *Zea Mays* and *Allium Cepa*, *Caryologia*, 2003, **56**(1), 65–73, DOI: **10.1080/00087114.2003.10589309**.

8 N. Tanibata, S. Takimoto, K. Nakano, H. Takeda, M. Nakayama and H. Sumi, Metastable Chloride Solid Electrolyte with High Formability for Rechargeable All-Solid-State Lithium Metal Batteries, *ACS Mater. Lett.*, 2020, **2**(8), 880–886, DOI: **10.1021/acsmaterialslett.0c00127**.

9 W. Weppner and R. A. Huggins, Ionic Conductivity of Solid and Liquid $LiAlCl_4$, *J. Electrochem. Soc.*, 1977, **124**(1), 35–38, DOI: **10.1149/1.2133238**.

10 B. C. Wood, J. B. Varley, K. E. Kweon, P. Shea, A. T. Hall, A. Grieder, M. Ward, V. P. Aguirre, D. Rigling, E. Lopez Ventura, C. Stancill and N. Adelstein, Paradigms of Frustration in Superionic Solid Electrolytes, *Philos. Trans. R. Soc., A*, 2021, **379**(2211), 20190467, DOI: **10.1098/rsta.2019.0467**.

11 T. P. Poudel, M. J. Deck, P. Wang and Y.-Y. Hu, Transforming Li3PS4 Via Halide Incorporation: A Path to Improved Ionic Conductivity and Stability in All-Solid-State Batteries, *Adv. Funct. Mater.*, 2024, **34**(4), 2309656, DOI: **10.1002/adfm.202309656**.

12 D. Karabelli, K. P. Birke and M. Weeber, A Performance and Cost Overview of Selected Solid-State Electrolytes: Race between Polymer Electrolytes and Inorganic Sulfide Electrolytes, *Batteries*, 2021, **7**(18), 1–13, DOI: **10.3390/batteries7010018**.

13 S. V. Patel, S. Banerjee, H. Liu, P. Wang, P.-H. Chien, X. Feng, J. Liu, S. P. Ong and Y.-Y. Hu, Tunable Lithium-Ion Transport in Mixed-Halide Argyrodites $Li_{6-x}PS_{5-x}ClBr_x$: An Unusual Compositional Space, *Chem. Mater.*, 2021, **33**(4), 1435–1443, DOI: **10.1021/acs.chemmater.0c04650**.

14 X. Feng, P.-H. Chien, Z. Zhu, I.-H. Chu, P. Wang, M. Immediato-Scuotto, H. Arabzadeh, S. P. Ong and Y.-Y. Hu, Studies of Functional Defects for Fast Na-Ion Conduction in Na3−*y*PS4−*x*Cl*x* with a Combined Experimental and Computational Approach, *Adv. Funct. Mater.*, 2019, **29**(9), 1807951, DOI: **10.1002/adfm.201807951**.

15 A. Shastri, N. Rons, Q.-P. Ding, S. J. Kmiec, M. Olson, Y. Furukawa and S. W. Martin, The Novel Oxy-Sulfide Glassy Ionic Conductors Na4P2S7-*x*O*x* $0 \leq x \leq 7$: Understanding the Features of Static and Dynamic Cations, *Solid State Ionics*, 2023, **402**, 116363, DOI: **10.1016/j.ssi.2023.116363**.

16 M. Olson, S. Kmiec and S. W. Martin, NaPON Doping of Na4P2S7 Glass and Its Effects on the Structure and Properties of Mixed Oxy-Sulfide-Nitride Phosphate Glass, *Inorg. Chem.*, 2022, **61**(44), 17469–17484, DOI: **10.1021/acs.inorgchem.2c02300**.

17 M. J. Deck, P.-H. Chien, T. P. Poudel, Y. Jin, H. Liu and Y.-Y. Hu, Oxygen-Induced Structural Disruption for Improved Li+ Transport and Electrochemical Stability of Li_3PS_4, *Adv. Energy Mater.*, 2024, **14**(4), 2302785, DOI: **10.1002/aenm.202302785**.

18 Q. Zhang, W. Arnold, Z. D. Hood, Y. Li, R. DeWees, M. Chi, Z. Chen, Y. Chen and H. Wang, $Li_{0.625}Al_{0.125}H_{0.25}Cl_{0.75}O_{0.25}$ Superionic Conductor with Disordered Rock-Salt Structure, *ACS Appl. Energy Mater.*, 2021, **4**(8), 7674–7680, DOI: **10.1021/acsaem.1c01011**.

19 X. Li, J. T. Kim, J. Luo, C. Zhao, Y. Xu, T. Mei, R. Li, J. Liang and X. Sun, Structural Regulation of Halide Superionic Conductors for All-Solid-State Lithium Batteries, *Nat. Commun.*, 2024, **15**(53), 1–8, DOI: **10.1038/s41467-023-43886-9**.

20 G. Kresse and J. Furthmüller, Efficient Iterative Schemes for *Ab Initio* Total-Energy Calculations Using a Plane-Wave Basis Set, *Phys. Rev. B*, 1996, **54**(16), 11169–11186, DOI: **10.1103/PhysRevB.54.11169**.

21 P. E. Blöchl, Projector Augmented-Wave Method, *Phys. Rev. B:Condens. Matter Mater. Phys.*, 1994, **50**(24), 17953–17979, DOI: **10.1103/PhysRevB.50.17953**.

22 J. P. Perdew, K. Burke and M. Ernzerhof, Generalized Gradient Approximation Made Simple, *Phys. Rev. Lett.*, 1996, **77**(18), 3865–3868, DOI: **10.1103/PhysRevLett.77.3865**.

23 S. P. Ong, W. D. Richards, A. Jain, G. Hautier, M. Kocher, S. Cholia, D. Gunter, V. L. Chevrier, K. A. Persson and G. Ceder, Python Materials Genomics (Pymatgen): A Robust, Open-Source Python Library for Materials Analysis, *Comput. Mater. Sci.*, 2013, **68**, 314–319, DOI: **10.1016/j.commatsci.2012.10.028**.

24 Y. Wang, W. D. Richards, S. P. Ong, L. J. Miara, J. C. Kim, Y. Mo and G. Ceder, Design Principles for Solid-State Lithium Superionic Conductors, *Nature Mater.*, 2015, **14**(10), 1026–1031, DOI: **10.1038/nmat4369**.

25 S. Ohno, C. Rosenbach, G. F. Dewald, J. Janek and W. G. Zeier, Linking Solid Electrolyte Degradation to Charge Carrier Transport in the Thiophosphate-Based Composite Cathode toward Solid-State Lithium-Sulfur Batteries, *Adv. Funct. Mater.*, 2021, **31**(18), 2010620, DOI: **10.1002/adfm.202010620**.

26 J. Gamon, M. S. Dyer, B. B. Duff, A. Vasylenko, L. M. Daniels, M. Zanella, M. W. Gaultois, F. Blanc, J. B. Claridge and M. J. Rosseinsky, $Li_{4.3}AlS_{3.3}Cl_{0.7}$: A Sulfide–Chloride

Lithium Ion Conductor with Highly Disordered Structure and Increased Conductivity, *Chem. Mater.*, 2021, **33**(22), 8733–8744, DOI: **10.1021/acs.chemmater.1c02751**.

27 L. A. Huff, J. L. Rapp, J. A. Baughman, P. L. Rinaldi and A. A. Gewirth, Identification of Lithium–Sulfur Battery Discharge Products through ^{6}Li and ^{33}S Solid-State MAS and ^{7}Li Solution NMR Spectroscopy, *Surf. Sci.*, 2015, **631**, 295–300, DOI: **10.1016/j.susc.2014.07.027**.

28 M. J. Deck and Y.-Y. Hu, Leveraging Local Structural Disorder for Enhanced Ion Transport, *J. Mater. Res.*, 2023, **38**(10), 2631–2644, DOI: **10.1557/s43578-023-01023-8**.

29 N. Bloembergen, E. M. Purcell and R. V. Pound, Relaxation Effects in Nuclear Magnetic Resonance Absorption, *Phys. Rev.*, 1948, **73**(7), 679–712, DOI: **10.1103/PhysRev.73.679**.

30 N. Wu, P. Chien, Y. Qian, Y. Li, H. Xu, N. S. Grundish, B. Xu, H. Jin, Y. Hu, G. Yu and J. B. Goodenough, Enhanced Surface Interactions Enable Fast Li $^{+}$ Conduction in Oxide/Polymer Composite Electrolyte, *Angew. Chem., Int. Ed.*, 2020, **59**(10), 4131–4137, DOI: **10.1002/anie.201914478**.

31 J. Zheng and Y.-Y. Hu, New Insights into the Compositional Dependence of Li-Ion Transport in Polymer–Ceramic Composite Electrolytes, *ACS Appl. Mater. Interfaces*, 2018, **10**(4), 4113–4120, DOI: **10.1021/acsami.7b17301**.

32 P. Wang, H. Liu, S. Patel, X. Feng, P.-H. Chien, Y. Wang and Y.-Y. Hu, Fast Ion Conduction and Its Origin in $Li_{6-x}PS_{5-x}Br_{1+x}$, *Chem. Mater.*, 2020, **32**(9), 3833–3840, DOI: **10.1021/acs.chemmater.9b05331**.

33 J. Zheng, H. Dang, X. Feng, P.-H. Chien and Y.-Y. Hu, Li-Ion Transport in a Representative Ceramic–Polymer–Plasticizer Composite Electrolyte: $Li_7La_3Zr_2O_{12}$ –Polyethylene Oxide–Tetraethylene Glycol Dimethyl Ether, *J. Mater. Chem. A*, 2017, **5**(35), 18457–18463, DOI: **10.1039/C7TA05832B**.

34 J. Zheng, M. Tang and Y. Hu, Lithium Ion Pathway within $Li_7La_3Zr_2O_{12}$ -Polyethylene Oxide Composite Electrolytes, *Angew., Chem. Int. Ed.*, 2016, **55**(40), 12538–12542, DOI: **10.1002/anie.201607539**.

35 Y. Gao, A. M. Nolan, P. Du, Y. Wu, C. Yang, Q. Chen, Y. Mo and S.-H. Bo, Classical and Emerging Characterization Techniques for Investigation of Ion Transport Mechanisms in Crystalline Fast Ionic Conductors, *Chem. Rev.*, 2020, **120**(13), 5954–6008, DOI: **10.1021/acs.chemrev.9b00747**.

36 G. F. Dewald, S. Ohno, M. A. Kraft, R. Koerver, P. Till, N. M. Vargas-Barbosa, J. Janek and W. G. Zeier, Experimental Assessment of the Practical Oxidative Stability of Lithium Thiophosphate Solid Electrolytes, *Chem. Mater.*, 2019, **31**(20), 8328–8337, DOI: **10.1021/acs.chemmater.9b01550**.

37 D. H. S. Tan, E. A. Wu, H. Nguyen, Z. Chen, M. A. T. Marple, J.-M. Doux, X. Wang, H. Yang, A. Banerjee and Y. S. Meng, Elucidating Reversible Electrochemical Redox of Li_6PS_5Cl Solid Electrolyte, *ACS Energy Lett.*, 2019, **4**(10), 2418–2427, DOI: **10.1021/acsenergylett.9b01693**.

38 Y. Tian, T. Shi, W. D. Richards, J. Li, J. Chul Kim, S.-H. Bo and G. Ceder, Compatibility Issues between Electrodes and Electrolytes in Solid-State Batteries, *Energy Environ. Sci.*, 2017, **10**(5), 1150–1166, DOI: **10.1039/C7EE00534B**.

39 F. Han, Y. Zhu, X. He, Y. Mo and C. Wang, Electrochemical Stability of $Li_{10}GeP_2S_{12}$ and $Li_7La_3Zr_2O_{12}$ Solid Electrolytes, *Adv. Energy Mater.*, 2016, **6**, 1501590, DOI: **10.1002/aenm.201501590**.

40 Y. Chen, P. Wang, E. Truong, B. Ogbolu, Y. Jin, I. Oyekunle, H. Liu, M. M. Islam, T. Poudel, C. Huang, I. Hung, Z. Gan and Y.-Y. Hu, Superionic Conduction in K_3SbS_4 Enabled by Cl-Modified Anion Lattice, *Angew. Chem., Int. Ed.*, 2024, **63**(35), e202408574, DOI: **10.1002/anie.202408574**.

41 S. Wang, R. Fang, Y. Li, Y. Liu, C. Xin, F. H. Richter and C.-W. Nan, Interfacial Challenges for All-Solid-State Batteries Based on Sulfide Solid Electrolytes, *J. Materiomics*, 2021, **7**(2), 209–218, DOI: **10.1016/j.jmat.2020.09.003**.

42 A. D. Bui, S.-H. Choi, H. Choi, Y.-J. Lee, C.-H. Doh, J.-W. Park, B. G. Kim, W.-J. Lee, S.-M. Lee and Y.-C. Ha, Origin of the Outstanding Performance of Dual Halide Doped $Li_7P_2S_8X$ (X = I, Br) Solid Electrolytes for All-Solid-State Lithium Batteries, *ACS Appl. Energy Mater.*, 2021, **4**(1), 1–8, DOI: **10.1021/acsaem.0c02321**.

43 S. Banerjee, M. L. Holekevi Chandrappa and S. P. Ong, Role of Critical Oxygen Concentration in the β-$Li_3PS_{4-x}O_x$ Solid Electrolyte, *ACS Appl. Energy Mater.*, 2022, **5**(1), 35–41, DOI: **10.1021/acsaem.1c03795**.

44 S. Wang, Q. Bai, A. M. Nolan, Y. Liu, S. Gong, Q. Sun and Y. Mo, Lithium Chlorides and Bromides as Promising Solid-State Chemistries for Fast Ion Conductors with Good Electrochemical Stability, *Angew. Chem., Int. Ed.*, 2019, **58**(24), 8039–8043, DOI: **10.1002/anie.201901938**.

45 W. D. Richards, L. J. Miara, Y. Wang, J. C. Kim and G. Ceder, Interface Stability in Solid-State Batteries, *Chem. Mater.*, 2016, **28**(1), 266–273, DOI: **10.1021/acs.chemmater.5b04082**.

46 J. Qu, J. Xiao, T. Wang, D. Legut and Q. Zhang, High Rate Transfer Mechanism of Lithium Ions in Lithium–Tin and Lithium–Indium Alloys for Lithium Batteries, *J. Phys. Chem. C*, 2020, **124**(45), 24644–24652, DOI: **10.1021/acs.jpcc.0c07880**.

47 P. Minnmann, L. Quillman, S. Burkhardt, F. H. Richter and J. Janek, Editors' Choice—Quantifying the Impact of Charge Transport Bottlenecks in Composite Cathodes of All-Solid-State Batteries, *J. Electrochem. Soc.*, 2021, **168**(4), 040537, DOI: **10.1149/1945-7111/abf8d7**.

48 D. Y. Oh, Y. E. Choi, D. H. Kim, Y.-G. Lee, B.-S. Kim, J. Park, H. Sohn and Y. S. Jung, All-Solid-State Lithium-Ion Batteries with TiS2 Nanosheets and Sulphide Solid Electrolytes, *J. Mater. Chem. A*, 2016, **4**(26), 10329–10335, DOI: **10.1039/C6TA01628F**.

49 B. R. Shin, Y. J. Nam, J. W. Kim, Y.-G. Lee and Y. S. Jung, Interfacial Architecture for Extra Li+ Storage in All-Solid-State Lithium Batteries, *Sci. Rep.*, 2014, **4**(1), 5572, DOI: **10.1038/srep05572**.